Nanoscale

PAPER

View Article Online
View Journal | View Issue

Cite this: *Nanoscale*, 2014, **6**, 4758

Strongly coupled hybrid nanostructures for selective hydrogen detection – understanding the role of noble metals in reducing cross-sensitivity†

Bin Liu,[a] Daoping Cai,[b] Yuan Liu,[a] Dandan Wang,[a] Lingling Wang,[a] Wuyuan Xie,[c] Qiuhong Li*[a] and Taihong Wang*[a]

Noble metal–semiconductor hybrid nanostructures can offer outperformance to gas sensors in terms of sensitivity and selectivity. In this work, a catalytically activated (CA) hydrogen sensor is realized based on strongly coupled Pt/Pd–WO_3 hybrid nanostructures constructed by a galvanic replacement participated solvothermal procedure. The room-temperature operation and high selectivity distinguish this sensor from the traditional ones. It is capable of detecting dozens of parts per million (ppm) hydrogen in the presence of thousands of ppm methane gas. An insight into the role of noble metals in reducing cross-sensitivity is provided by comparing the sensing properties of this sensor with a traditional thermally activated (TA) one made from the same pristine WO_3. Based on both experimental and density functional theory (DFT) calculation results, the cross-sensitivity of the TA sensor is found to have a strong dependence on the highest occupied molecular orbital (HOMO) level of the hydrocarbon molecules. The high selectivity of the CA sensor comes from the reduced impact of gas frontier orbitals on the charge transfer process by the nano-scaled metal–semiconductor (MS) interface. The methodology demonstrated in this work indicates that rational design of MS hybrid nanostructures can be a promising strategy for highly selective gas sensing applications.

Received 11th December 2013
Accepted 11th February 2014

DOI: 10.1039/c3nr06569c

www.rsc.org/nanoscale

Introduction

The selective detection of certain target gases is critically important for pollution monitoring, public safety assurance and personal healthcare.[1–3] Metal oxide semiconductor (MOS) based gas sensors have attracted considerable attention due to their high sensitivity, low cost, small size and easy implementation.[4–7] In recent years, nanostructures with various morphologies have been extensively investigated for gas sensing applications, which has provided profound insights into the sensing mechanism.[7–16] Taking advantage of the scale effect and grain boundary effect, low detection limits and fast response speeds have been achieved.[17–19] The lower detection limits of most volatile organic compounds (VOCs) have been reduced to the ppm level which is usually far below the lower explosive limit (LEL).[20,21] But most of these parameters are obtained under ideal conditions, including optimized working temperatures, high purity target gases and abundant energy supplies. In real world applications there are many restrictions, and a very representative example is the detection of hydrogen in oil refineries. Containing high concentrations of hydrocarbon gases, the hydrogen sensing signal can be easily disturbed. Technically speaking, the one-dimensional information given by the response of a sensor is inadequate to know the gas and its concentration at the same time if interfering gases are present.[22,23] Various techniques such as doping,[24] surface modification[25,26] and facet engineering[27,28] have been developed to reduce the cross-sensitivity of gas sensors. Among them, constructing MS hybrid nanostructures has shown promising applications in selective gas detection through the novel chemical and electronic interactions between the metal and semiconductor.[11,29–31]

The creation of MS nanostructures has been realized by a series of physical and chemical methods.[32] Physical methods such as thermal evaporation and sputtering can deposit highly pure metals on semiconductors. They are particularly useful when the hybrid nanostructures are prepared on substrates but seem powerless for materials in the powder form.[33] In contrast, wet chemical methods are simple, cost-effective and especially suitable for powder materials. The simplest approach is to mix pre-synthesized noble metal nanocrystals with the semiconductor dispersion.[34,35] But this mixing strategy often suffers from loose attachments of the noble metals to the semiconductor substrate, which results in performance degradation.[36] Here, we describe

[a]*Pen-Tung Sah Institute of Micro-Nano Science and Technology of Xiamen University, Xiamen, 361005, China. E-mail: liqiuhong2004@hotmail.com; thwang@xmu.edu.cn*

[b]*Department of Chemistry, College of Chemistry and Chemical Engineering, Xiamen University, Xiamen, 361005, China*

[c]*Department of Physics, School of Physics and Mechanical & Electrical Engineering, Xiamen University, Xiamen, 361005, China*

† Electronic supplementary information (ESI) available. See DOI: 10.1039/c3nr06569c

the fabrication of room temperature hydrogen sensors based on bimetallic Pt/Pd nanocube (NC) and WO_3 nanoplate (NP) formed hybrid nanostructures. Unlike previous fabrication procedures, the hollow Pt/Pd NCs are directly grown on the surface of WO_3 using a solvothermal method. As demonstrated by our recent studies,[25,37] a strong coupling between the noble metal nanocrystal and the metal oxide support is important to guarantee a high sensing performance. Compared with the traditional TA sensors, the CA sensor exhibits high sensitivity and selectivity to hydrogen. The interesting differences between them are interpreted on the basis of both experimental and calculation results.

Results and discussion

The WO_3 NPs were synthesized using an organic acid assisted hydrothermal method. The X-ray diffraction pattern (Fig. S1†) shows that all the peaks of the product can be indexed to the monoclinic phase of WO_3 (JCPDS no. 83-0950), indicating the high phase purity. Scanning electron microscopy (SEM) observations show that the WO_3 NPs display a square plate-like morphology with an edge-to-edge width of about 150 nm (Fig. 1b) and a thickness of 20–30 nm (Fig. 1c). Fig. 1d shows the typical transmission electron microscopy (TEM) image of the WO_3 NPs. As the role of the organic acid during the formation of the square plate-like WO_3 nanostructures has been extensively discussed in previous studies,[38,39] the morphology evolution as a function of HCl concentration was investigated by control experiments. If the reaction was carried out without HCl, no solid products were found after the reaction. As shown in Fig. S2,† upon adding 0.1 mL of hydrochloric acid (36% w/w), irregular shaped plate-like products were obtained. With increasing HCl concentration, the shape of the WO_3 NPs became more and more regular. This result implied that HCl was not only the precipitating agent but also played a synergistic role with the organic acid in controlling the morphology of the final products. However, the impact of HCl was much reduced, as the amount of hydrochloric acid was more than 0.5 mL. The WO_3 NPs used in the following parts of this work were synthesized by adding 1.0 mL of hydrochloric acid.

The direct growth of the hollow Pt/Pd NCs on WO_3 NPs was realized using a one-pot solvothermal method. First investigated by Zheng *et al.*, the galvanic replacement of palladium atoms by platinum(II) was identified as the main driving force to create this novel hollow structure by just a one-pot reaction.[40,41] Fig. 2a and b are the TEM images of the hybrid nanostructures. It is worth noting that most Pt/Pd NCs are directly attached to the surface of the WO_3 NPs. This is ascribed to the fact that the addition of WO_3 NPs to the reacting solution creates heterogeneous solid–liquid interfaces for the nucleation.[42] Fig. 2c shows the hollow Pt/Pd NCs which are about 10–15 nm in dimensions. The single-crystalline nature of the bimetallic NCs is revealed by the continuous lattice fringes oriented in the same direction across the whole cube in Fig. S3b.† The lattice parameters of the NCs were determined by analyzing the lattice plane spacing in the HRTEM image. The lattice distance of 0.195 nm is between the {200} interplanar distance of face centred cubic (fcc) palladium (0.194 nm) and platinum (0.196 nm); so it is identified as the {200} interplanar distance of this bimetallic alloy. The hollow feature is revealed by both TEM observation and the Energy Dispersive X-ray (EDX) elemental line scanning profile across a single nanocube in Fig. 2d. As for the composition of the alloy, determined by the EDX quantification results, the hollow NCs contain 54% Pd and 46% Pt (atomic ratio, Fig. S4†), which is very close to the theoretical value (52% Pd and 48% Pt). The percentages of Pd and Pt in the hybrid nanostructures are 5.9% and 9.3% by weight, respectively.

Hydrogen sensors were fabricated on the alumina ceramic substrate with predefined Au interdigitated electrodes (IDEs). Gas sensing tests were carried out with a ZhongKe NS-4003

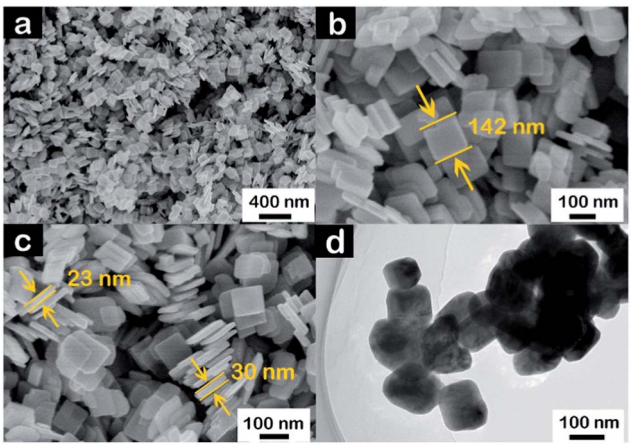

Fig. 1 (a–c) SEM images of the WO_3 NPs. The representative width and thickness of the products are marked in (b) and (c), respectively. (d) A typical TEM image showing the dimensions of the WO_3 NPs.

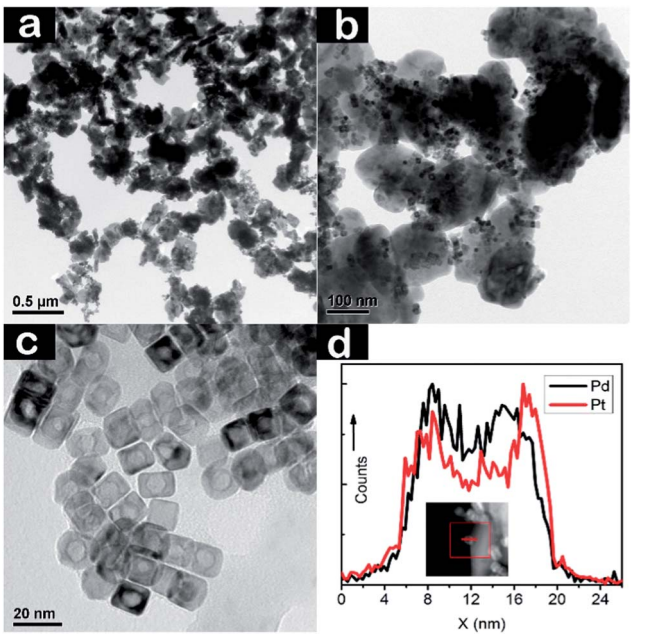

Fig. 2 (a and b) TEM images of the Pt/Pd–WO_3 hybrid nanostructure. (c) High magnification TEM image of the hollow Pt/Pd NCs. (d) EDX line-scanning profile of a single Pt/Pd nanocube showing its hollow feature.

smart sensor analyser. The CA sensor exhibited a fast and high response to hydrogen at room temperature but the TA sensor did not show any response under the same conditions. However, an obvious response of the TA sensor to hydrogen was observed by applying a heating voltage of 5 V (the corresponding working temperature was about 350 °C). Fig. 3 displays the dynamic sensing transients of the two sensors obtained by exposing them to various concentrations of hydrogen gas. The gas response R was defined as $R = R_a/R_g$, in which R_a and R_g were the resistances of the sensor in air and in the target gas, respectively. And the time it consumed for the sensor to reach 90% of the resistance change after a step change in the gas concentration was defined as the response time τ_{res}. At a relatively low concentration of 0.05 vol%, the CA sensor exhibited a higher response ($R = 4$) than the TA sensor ($R = 1.7$), but the latter had a much faster response speed (τ_{res} values of the CA and TA sensor were 70 and 23 s, respectively). With increasing hydrogen concentration, τ_{res} of the CA sensor decreased sharply, from 70 s at 0.05 vol% to 8 s at 0.4 vol%, while that of the TA sensor only decreased from 23 to 11 s. This difference was most probably caused by the fundamentally different sensing mechanisms. For the TA sensor, the charge transfer was caused by direct reactions between hydrogen and the absorbed oxygen species (O_2^-, O^-, O^{2-}) on the surface of WO_3.[43] Accelerated by the thermal activation, chemical equilibrium could be quickly reached. While for the CA sensor, dissociation of hydrogen molecules into more active hydrogen atoms was essential since the reaction between hydrogen molecules and the ionized oxygen can hardly take place at room temperature. As the response speed of the CA sensor ($\tau_{res} = 8$ s) was even faster than that of the TA sensor ($\tau_{res} = 10$ s) under a relatively high concentration of 0.4 vol%, it could be speculated that the response speed of the CA sensor was not limited by the hydrogen dissociation ability of the Pt/Pd NCs but by the slow uptake of hydrogen at low concentrations.

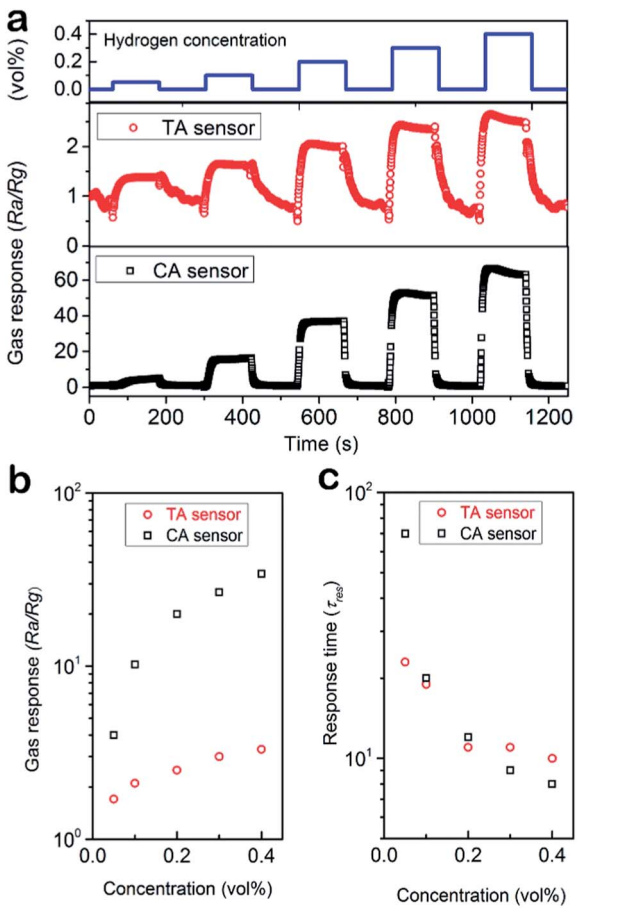

Fig. 3 (a) Transient response curves of the TA and CA sensor to different concentrations of hydrogen. Gas-sensing response (b) and response time (c) of the two sensors *versus* hydrogen concentration.

In order to investigate the role of MS interactions on the oxygen adsorption process, a slight thermal shock (rapid heating from room temperature to about 80 °C) was applied to both sensors with their real-time resistance being monitored in an air atmosphere. The corresponding resistance change is shown in Fig. S5.† Interestingly, the two sensors displayed totally different responses to the thermal shock. A sharp decrease in the resistance of the TA sensor was observed immediately after the thermal shock. It is known that WO_3 is an n-type semiconductor due to the oxygen vacancies, meaning the majority carriers in WO_3 are electrons. The thermal shock broke the equilibrium between the thermal excitation of electrons from the electron-occupied donors to the conduction band and the capture of electrons into empty donors. The increased conductance at the first stage was ascribed to the sudden increase in the number of electrons through thermal excitation:

$$V_0 \xleftrightarrow{kT} V_0^{\gamma+} + \gamma e^- \quad (1)$$

where V_0 stands for an electron-occupied donor state; it can get partially ($\gamma = 1$) or fully ($\gamma = 2$) ionized at high temperatures. The presence of an obvious recovery process indicated that the elevated temperature also promoted the chemisorption of oxygen. The oxygen ions captured electrons from the conduction band and made the WO_3 surface depleted. It took about 90 s for the resistance to reach equilibrium. In contrast, the resistance of the CA sensor increased by about tenfold in less than 10 s and quickly reached equilibrium. This result suggested that the Pt/Pd NCs played an important role in accelerating and enhancing the chemisorption of oxygen. So the role of the Pt/Pd NCs in improving the response (R_a/R_g) is a combined effect of promoting oxygen adsorption in air (larger R_a) and enhancing hydrogen dissociation in the target gas (smaller R_g).

Five common gaseous hydrocarbons, methane (CH_4), acetylene (C_2H_2), ethane (C_2H_6), propane (C_3H_8) and *n*-butane (C_4H_{10}) were used as probe molecules to investigate the cross-sensitivity of the two sensors. The CA sensor based on the hybrid nanostructures did not show any detectable response to these hydrocarbon gases, indicating its high selectivity to hydrogen. In contrast, the TA sensor displayed response to all these gases. Fig. 4 shows the transient response curves of the TA sensor to different hydrocarbons. A very interesting thing was that the response to C_2H_2 was obviously much higher than that to all the other gases of the same concentration. For example, the response to 0.1 vol% CH_4, C_2H_2, C_2H_6, C_3H_8 and C_4H_{10} was 5.5, 12.1, 5.8,

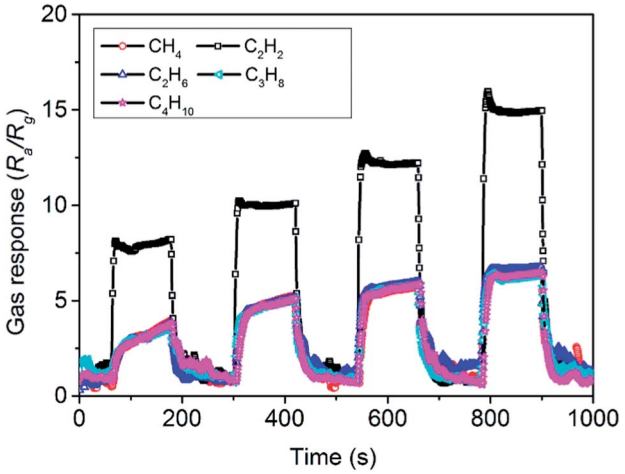

Fig. 4 Transient responses of the TA sensor to the hydrocarbon gases, the corresponding concentrations are 0.02, 0.05, 0.1 and 0.2 vol%, respectively.

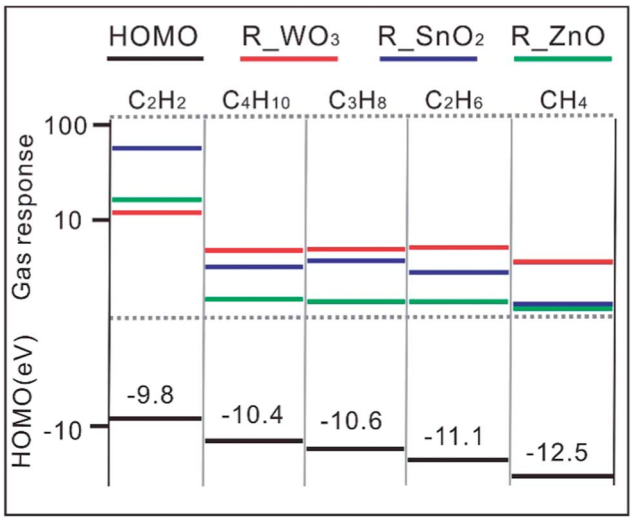

Fig. 5 Gas-sensing responses of the three TA sensors to different hydrocarbon gases and the corresponding HOMO energy levels obtained by DFT calculations.

5.7 and 5.6, respectively. In order to get a deeper understanding of the nature of cross-sensitivity, another two TA sensors were fabricated and their sensing properties towards these hydrocarbon gases were investigated. The gas sensing transients of the ZnO (Fig. S6a†) and SnO_2 (Fig. S6b†) based TA sensors to hydrocarbons are shown in Fig. S7a and S7b,† respectively. The response of the three sensors toward one specific gas could be very different. For example, the response of the sensors based on WO_3, ZnO and SnO_2 to 0.1 vol% C_2H_2 was 12.1, 20.1 and 77.7, respectively. But all of them exhibited the highest response to C_2H_2 and the lowest to CH_4. This result indicated that for the thermally activated sensors, to a great extent the so-called selectivity was not only dependent on the sensing materials but also decided by some properties of the target gas itself.

Based on the molecular frontier orbital theory, a large number of molecular properties were decided by the frontier molecular orbitals (FMOs), especially the highest occupied molecular orbital (HOMO) and lowest unoccupied molecular orbital (LUMO).[44] In this regard, geometry and energy optimisations were carried out for the above hydrocarbon molecules using DFT with the CAM-B3LYP functional and the 6-311G basis set. All the calculations were conducted using the Gaussian03 computational package. As shown in Fig. 5 and Table S1,† the HOMO energy level of C_2H_2, C_4H_{10}, C_3H_8, C_2H_6, CH_4 is −9.8, −10.4, −10.6, −11.1 and −12.5 eV, respectively. C_2H_2 possessed the highest HOMO among the five hydrocarbon gases, and all the TA sensors exhibited the highest response towards it. In fact, taking the inevitable interference of the experimental environments such as small fluctuations in temperature and gas mixing homogeneity into consideration, the response of all three sensors displayed a strong dependence on the HOMO energy of the hydrocarbon gas. Based on the adsorption–reaction–desorption model of gas sensors,[20,45] reducing gases react as electron donors in the surface reaction. Since electrons from the HOMO are most free to participate in the reaction, the position of the HOMO level has a strong influence on the response. Although each sensor may have an optimized working temperature for a specific gas, we can conclude from the present result that the effect of thermal activation is quite universally valid for different gases.

The differences between the charge transfer dynamics of the TA and CA sensor are schematically shown in Fig. 6. Stage A represents a WO_3 nanoplate under an air atmosphere at room temperature, where a small quantity of oxygen is chemisorbed mainly in the molecular form:[46]

$$O_{2(gas)} \Leftrightarrow O_{2(ads)} \quad (2)$$

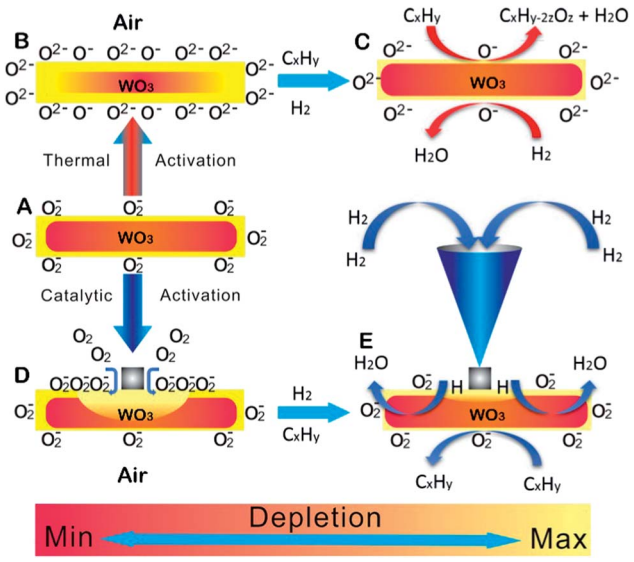

Fig. 6 Schematic diagram of the charge transfer mechanisms of the TA and CA sensor. (A) WO_3 NPs in air at room temperature. (B) TA WO_3 NPs in air at high temperatures. (C) TA WO_3 NPs under hydrogen and hydrocarbon gases. (D) CA WO_3 NPs in air at room temperature. (E) CA WO_3 NPs under hydrogen and hydrocarbon gases at room temperature.

$$O_{2(ads)} + e^- \Leftrightarrow O_{2(ads)}^- \quad (3)$$

In this stage, the negatively ionized oxygen is less active, which results in no response to either hydrogen or hydrocarbons. Under thermal activation, the oxygen molecules are dissociated into more active oxygen ions:

$$O_{2(ads)}{}^- + e^- \overset{kT}{\Leftrightarrow} 2O_{(ads)}{}^- \quad (4)$$

$$O_{2(ads)}{}^- + 3e^- \overset{kT}{\Leftrightarrow} 2O_{(ads)}{}^{2-} \quad (5)$$

The oxygen dissociation induced by thermal activation is represented by eqn (4) and (5), which captures electrons from the conduction band of WO_3, leading to deeper electron depletion (Stage B in Fig. 6). Similarly, as illustrated by Stage D, the catalytic activation also enhances the chemisorption of oxygen. Previous studies mainly focus on the functionalization of noble metals which is known as the spillover effect.[11,47] In fact, from an electronic point of view, the interaction between the metal and the semiconductor support is mutual. The height of the energy barrier (Schottky barrier) formed at an ideal MS interface is given by:[48]

$$\phi_{bn} = \Phi_m - \chi \quad (6)$$

where Φ_{bn} is the Schottky barrier height to an n-type semiconductor, Φ_m is the work function of the metal and χ is the electron affinity of the semiconductor. In this case, since the work functions of Pd and Pt (5.3 and 7.0 eV respectively for the {100} facet)[49] are much larger than the electron affinity of WO_3 (3.3 eV),[50] the net electron transfer from the semiconductor to metal will take place if the Pt/Pd NCs and WO_3 NPs come into contact, forming the "nano-Schottky junction" at the MS interface.[11] Recent studies have shown that such semiconductor supports acting as an "electron bath" can greatly enhance the catalytic performance of noble metal nanocrystals.[51,52] The synergy between the metal and semiconductor offers better performance to the hybrid sensor than those made from semiconductors or even pure noble metals.[53]

As hydrogen and other hydrocarbon gases are introduced, the adsorbed oxygen on the TA WO_3 NPs reacts with these reducing gases. The electrons trapped by the oxygen ions are released back to the conduction band as shown in Stage C in Fig. 6. The populated free electrons cause the depletion layer to decrease, resulting in a significant increase of the conductance. The oxygen ions on the TA WO_3 NPs seem to be highly active since hydrogen or any of the hydrocarbon gases can induce an obvious response. In contrast, the charge transfer in the CA sensor is controlled by a totally different reaction path. As shown in Stage E of Fig. 6, first hydrogen molecules must be dissociated into more active hydrogen atoms and then their reaction with oxygen ions can take place at room temperature.

As mentioned above, the CA sensor did not show any response to any of the hydrocarbon gases. We also examined whether this sensor could respond to very dilute hydrogen in the presence of high concentrations of hydrocarbons. As shown in Fig. 7, 5000 ppm CH_4 was introduced into the test chamber at t = 60 s. The resistance of the sensor remained almost unchanged in the following 60 s before 20 ppm hydrogen was introduced at t = 120 s. The response was not obvious until t = 130 s because it took some time for hydrogen gas to diffuse from the inlet port to the sensor. The resistance of the CA sensor decreased by over 10% in 5 min under 20 ppm hydrogen. The responses to 50 and 100 ppm hydrogen were as high as 36% and 82%, indicating the high potential of the CA sensor for selective detection of hydrogen in a highly complex ambient background. The highly selective sensors may also find their use in hydrogen production as a replacement of the expensive gas chromatography technique,[54,55] which is very important for hydrogen energy development.

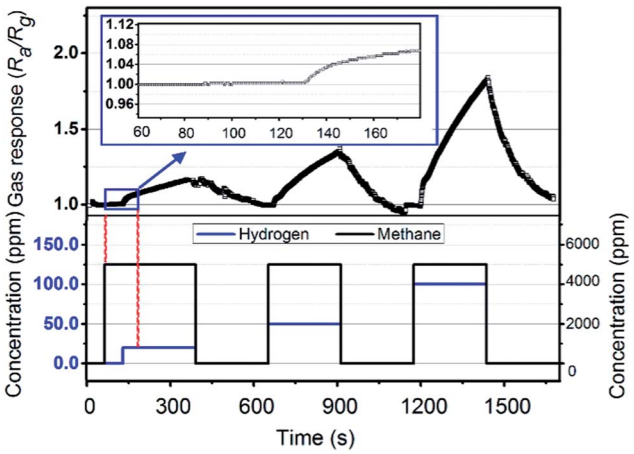

Fig. 7 Dynamic response curve of the CA sensor to hydrogen in the presence of methane. The inset shows the real-time response of the sensor by introducing 5000 ppm methane at t = 60 s and 20 ppm hydrogen at t = 120 s.

Methods

Synthesis of WO_3 NPs

In a typical synthesis procedure, 0.25 g of $Na_2WO_4 \cdot 2H_2O$ and 0.15 g of citric acid were added into a 25 mL Teflon liner containing 15 mL of distilled water. Afterwards, 1 mL of hydrochloric acid (36%, w/w) was added slowly into the mixture under intense ultrasonication. Then the autoclave was sealed and kept in an electronic oven at 120 °C for 1440 min. After cooling down to room temperature, the yellow precipitates were washed with distilled water and ethanol each for 3 times and then dried in an electronic oven at 70 °C. The dry precipitates were annealed in a muffle furnace to remove any possible organic residue and get better crystallinity. The temperature was increased from room temperature to 600 °C with a heating rate of 5 °C min^{-1} and maintained at 600 °C for 2 h before cooling to ambient temperature spontaneously. Then the final products were collected for further characterization and sensor fabrication.

Construction of the hybrid nanostructures

The hybrid nanostructures were synthesized using a solvothermal method. In a typical experiment, 25 mg of palladium

acetylacetonate [$Pd(acac)_2$], 30 mg of platinum acetylacetonate [$Pt(acac)_2$], 160 mg of polyvinylpyrrolidone (PVP, K30) and 0.36 g of $NaI \cdot 2H_2O$ were added to a 25 mL Teflon liner containing 10 mL of *N*,*N*-dimethylformamide (DMF) and 2 mL of distilled water. Then 100 mg of the annealed WO_3 NPs was added to the above mixture under ultrasonic treatment. Afterwards, the liner was sealed using a stainless crust and heated at 150 °C for 8 h. After cooling down to room temperature, the products were centrifuged and washed with ethanol 3 times.

Material characterization

The crystal structure of the WO_3 NPs was characterized by XRD patterns obtained with a Rigaku Ultima IV X-ray diffractometer using Cu Kα ($\lambda = 0.154$ nm) radiation at 35 kV and 15 mA. The morphologies of the WO_3 NPs and the hybrid nanostructures were observed using a scanning electron microscope (Hitachi S4800) and a transmission electron microscope (FEI Tecnai F30) operating at 300 kV. The EDX analyses were performed with an Oxford INCA Energy Dispersive Spectrometer.

Sensor fabrication

Al_2O_3 ceramic wafers (thickness = 0.5 mm) were used as the substrate for their low conductivity and high chemical stability. The IDEs were fabricated by sputtering a layer of gold (80 nm) on the top of an adhesion layer of titanium (10 nm) using a metal shadow mask with a predefined pattern. The CA sensor was fabricated by depositing the hybrid nanostructure dispersed in ethanol onto the pre-cleaned IDEs (Fig. S8, ESI†). The TA sensors were fabricated as follows: the WO_3 NPs were mixed with terpineol by grinding and then the mixture was coated onto an alumina tube with two Au electrodes. A Ni–Cr coil was inserted into the tube and it worked as the heater. The working temperature could be adjusted by changing the heating voltage.

Conclusions

In conclusion, we have demonstrated a simple but effective approach to synthesize strongly coupled Pt/Pd–WO_3 hybrid nanostructures constituted by hollow Pt/Pd bimetallic NCs and WO_3 NPs. The direct growth process and the local charge transfer at the MS interface enabled a strong coupling effect. Compared with the TA sensor based on pristine WO_3, the CA sensor based on the hybrid nanostructure exhibited fast response, high sensitivity and remarkable selectivity to hydrogen. It could respond to ppm level hydrogen in the presence of parts per thousand levels of methane. In addition, on the basis of both experimental and DFT calculation analyses, the thermal activation was found to result in a strong dependence of the response characteristics on the HOMO energy level of the target gas. The different sensing behaviours of the two sensors can be understood from an energy point of view. For the hot, highly active sensing system, the response depends more on the energy level diagram of the target gas; while for the cool, less active sensing system, it depends more on the intrinsic selectivity of the sensing element.

Acknowledgements

We thank the financial support from the National Natural Science Foundation of China (Grant no. 61376073).

References

1 K. A. Mirica, J. M. Azzarelli, J. G. Weis, J. M. Schnorr and T. M. Swager, *Proc. Natl. Acad. Sci. U. S. A.*, 2013, **110**, E3265–E3270.
2 J. Shin, S. J. Choi, I. Lee, D. Y. Youn, C. O. Park, J. H. Lee, H. L. Tuller and I. D. Kim, *Adv. Funct. Mater.*, 2013, **23**, 2357–2367.
3 Y. Yu, J. Zhang, X. Wu, W. Zhao and B. Zhang, *Angew. Chem., Int. Ed.*, 2012, **51**, 897–900.
4 F.-N. Meng, X.-P. Di, H.-W. Dong, Y. Zhang, C.-L. Zhu, C. Li and Y.-J. Chen, *Sens. Actuators, B*, 2013, **182**, 197–204.
5 B. Bouxin, K. Maier, A. Hackner, G. Mueller, F. Shao, J. D. Prades, F. Hernandez-Ramirez and J. R. Morante, *Sens. Actuators, B*, 2013, **182**, 25–30.
6 Q. W. Huang, D. W. Zeng, H. Y. Li and C. S. Xie, *Nanoscale*, 2012, **4**, 5651–5658.
7 Q. Wan, Q. H. Li, Y. J. Chen, T. H. Wang, X. L. He, J. P. Li and C. L. Lin, *Appl. Phys. Lett.*, 2004, **84**, 3654–3656.
8 Y.-J. Chen, X.-M. Gao, X.-P. Di, Q.-Y. Ouyang, P. Gao, L.-H. Qi, C.-Y. Li and C.-L. Zhu, *ACS Appl. Mater. Interfaces*, 2013, **5**, 3267–3274.
9 J. Ma, L. Mei, Y. Chen, Q. Li, T. Wang, Z. Xu, X. Duan and W. Zheng, *Nanoscale*, 2013, **5**, 895–898.
10 Y. F. Hu, J. Zhou, P. H. Yeh, Z. Li, T. Y. Wei and Z. L. Wang, *Adv. Mater.*, 2010, **22**, 3327–3332.
11 A. Kolmakov, D. O. Klenov, Y. Lilach, S. Stemmer and M. Moskovits, *Nano Lett.*, 2005, **5**, 667–673.
12 L. L. Fields, J. P. Zheng, Y. Cheng and P. Xiong, *Appl. Phys. Lett.*, 2006, **88**, 263102.
13 Y. S. Li, J. Xu, J. F. Chao, D. Chen, S. X. Ouyang, J. H. Ye and G. Z. Shen, *J. Mater. Chem.*, 2011, **21**, 12852–12857.
14 J. M. Ma, J. Zhang, S. R. Wang, T. H. Wang, J. B. Lian, X. C. Duan and W. J. Zheng, *J. Phys. Chem. C*, 2011, **115**, 25183.
15 D. L. Chen, X. X. Hou, H. J. Wen, Y. Wang, H. L. Wang, X. J. Li, R. Zhang, H. X. Lu, H. L. Xu, S. K. Guan, J. Sun and L. Gao, *Nanotechnology*, 2010, **21**, 035501.
16 N. Garg, A. Mohanty, N. Lazarus, L. Schultz, T. R. Rozzi, S. Santhanam, L. Weiss, J. L. Snyder, G. K. Fedder and R. C. Jin, *Nanotechnology*, 2010, **21**, 405501.
17 N. L. Wu, S. Y. Wang and I. A. Rusakova, *Science*, 1999, **285**, 1375–1377.
18 E. Comini, *Anal. Chim. Acta*, 2006, **568**, 28–40.
19 S. Hu and X. Wang, *Chem. Soc. Rev.*, 2013, **42**, 5577–5594.
20 A. Tricoli, M. Righettoni and A. Teleki, *Angew. Chem., Int. Ed.*, 2010, **49**, 7632–7659.
21 F. M. Yujin Chen, C. Ma, Z. Yang, C. Zhu, Q. Ouyang, P. Gao, J. Li and C. Sun, *J. Mater. Chem.*, 2012, **22**, 12900–12906.
22 S. Nakata and K. Kashima, *Anal. Methods*, 2012, **4**, 1126–1131.

23 K. T. Ng, F. Boussaid and A. Bermak, *IEEE Transactions on Circuits and Systems, I: Fundamental Theory and Applications*, 2011, **58**, 1569–1580.
24 S. Cui, Z. Wen, E. C. Mattson, S. Mao, J. Chang, M. Weinert, C. J. Hirschmugl, M. Gajdardziska-Josifovska and J. Chen, *J. Mater. Chem. A*, 2013, **1**, 4462.
25 B. Liu, D. Cai, Y. Liu, H. Li, C. Weng, G. Zeng, Q. Li and T. Wang, *Nanoscale*, 2013, **5**, 2505–2510.
26 C. W. Na, H. S. Woo, I. D. Kim and J. H. Lee, *Chem. Commun.*, 2011, **47**, 5148–5150.
27 X. G. Han, M. S. Jin, S. F. Xie, Q. Kuang, Z. Y. Jiang, Y. Q. Jiang, Z. X. Xie and L. S. Zheng, *Angew. Chem., Int. Ed.*, 2009, **48**, 9180–9183.
28 X. Han, L. Li and C. Wang, *Chem.–Asian J.*, 2012, **7**, 1572–1575.
29 F. Boccuzzi, G. Ghiotti and A. Chiorino, *Surf. Sci.*, 1987, **183**, L285–L289.
30 J. M. Baik, M. H. Kim, C. Larson, C. T. Yavuz, G. D. Stucky, A. M. Wodtke and M. Moskovits, *Nano Lett.*, 2009, **9**, 3980–3984.
31 X. Y. Xue, Z. H. Chen, C. H. Ma, L. L. Xing, Y. J. Chen, Y. G. Wang and T. H. Wang, *J. Phys. Chem. C*, 2010, **114**, 3968–3972.
32 S. T. Kochuveedu, Y. H. Jang and D. H. Kim, *Chem. Soc. Rev.*, 2013, **42**, 8467–8493.
33 A. P. Abiyasa, S. F. Yu, S. P. Lau, E. S. P. Leong and H. Y. Yang, *Appl. Phys. Lett.*, 2007, **90**, 231106.
34 S. T. Kochuveedu, J. H. Oh, Y. R. Do and D. H. Kim, *Chem.–Eur. J.*, 2012, **18**, 7467–7472.
35 J. J. Chen, J. C. S. Wu, P. C. Wu and D. P. Tsai, *J. Phys. Chem. C*, 2011, **115**, 210–216.
36 Q. Zhang, D. Q. Lima, I. Lee, F. Zaera, M. F. Chi and Y. D. Yin, *Angew. Chem., Int. Ed.*, 2011, **50**, 7088–7092.
37 B. Liu, D. Cai, Y. Liu, D. Wang, L. Wang, Y. Wang, H. Li, Q. Li and T. Wang, *Sens. Actuators, B*, 2014, **193**, 28–34.
38 X. T. Su, F. Xiao, Y. N. Li, J. K. Jian, Q. J. Sun and J. D. Wang, *Mater. Lett.*, 2010, **64**, 1232–1234.
39 B. Miao, W. Zeng, S. Xu, S. Zeng, Y. Chen and S. Wu, *Mater. Lett.*, 2013, **113**, 13–16.
40 X. Huang, H. Zhang, C. Guo, Z. Zhou and N. Zheng, *Angew. Chem.*, 2009, **48**, 4808–4812.
41 M. Chen, B. Wu, J. Yang and N. Zheng, *Adv. Mater.*, 2012, **24**, 862–879.
42 A. Engelbrecht, R. Meneses and H. J. Schope, *Soft Matter*, 2011, **7**, 5685–5690.
43 Z. Xie, Y. G. Zhu, J. Xu, H. T. Huang, D. Chen and G. Z. Shen, *CrystEngComm*, 2011, **13**, 6393–6398.
44 M. W. G. Hoffmann, J. D. Prades, L. Mayrhofer, F. Hernandez-Ramirez, T. T. Järvi, M. Moseler, A. Waag and H. Shen, *Adv. Funct. Mater.*, 2014, **24**, 595–602.
45 N. Yamazoe and K. Shimanoe, *Sens. Actuators, B*, 2008, **128**, 566–573.
46 D. P. Volanti, A. A. Felix, M. O. Orlandi, G. Whitfield, D.-J. Yang, E. Longo, H. L. Tuller and J. A. Varela, *Adv. Funct. Mater.*, 2013, **23**, 1759–1766.
47 S. Khoobiar, *J. Phys. Chem.*, 1964, **68**, 411–412.
48 W. Schottky, *Z. Physik*, 1942, **118**, 539–592.
49 H. L. Skriver and N. M. Rosengaard, *Phys. Rev. B: Condens. Matter Mater. Phys.*, 1992, **46**, 7157–7168.
50 C. W. Walter, C. F. Hertzler, P. Devynck, G. P. Smith and J. R. Peterson, *J. Chem. Phys.*, 1991, **95**, 824–827.
51 M. Cargnello, V. V. Doan-Nguyen, T. R. Gordon, R. E. Diaz, E. A. Stach, R. J. Gorte, P. Fornasiero and C. B. Murray, *Science*, 2013, **341**, 771–773.
52 Q. L. He, Y. H. Lai, Y. Lu, K. T. Law and I. K. Sou, *Sci. Rep.*, 2013, **3**, 2497.
53 F. Favier, E. C. Walter, M. P. Zach, T. Benter and R. M. Penner, *Science*, 2001, **293**, 2227–2231.
54 X. Wu, Y. Yu, Y. Liu, Y. Xu, C. Liu and B. Zhang, *Angew. Chem., Int. Ed.*, 2012, **51**, 3211–3215.
55 W. Z. Y. Xu, R. Xu, Y. Shi and B. Zhang, *Chem. Commun.*, 2013, **49**, 9803–9805.